Journal of Materials Chemistry C

Electrolytes for Reversible Zinc Electrodeposition for Dynamic Windows

Journal:	*Journal of Materials Chemistry C*
Manuscript ID	TC-ART-02-2021-000857.R1
Article Type:	Paper
Date Submitted by the Author:	13-Apr-2021
Complete List of Authors:	Madu, Desmond; University of Nevada, Reno, Department of Chemistry Islam, Shakirul; University of Nevada, Reno, Department of Chemistry Pan, Hanqing; University of Nevada, Reno, Department of Chemistry Barile, Christopher; University of Nevada, Reno, Department of Chemistry

Electrolytes for Reversible Zinc Electrodeposition for Dynamic Windows

Desmond C. Madu, Shakirul M. Islam, Hanqing Pan, and Christopher J. Barile*

Department of Chemistry, University of Nevada, Reno, NV 89557

*E-mail: cbarile@unr.edu

Abstract

Reversible metal electrodeposition is a promising approach for the construction of dynamic windows with electronically tunable transmission. In this manuscript, we study a series of aqueous electrolytes that support reversible Zn electrodeposition on transparent tin-doped indium oxide electrodes. By systematically altering the composition of the electrolytes, we develop relationships between the chemical identity of the halides, carboxylates, and haloacetates in the electrolytes and the electrochemical and optical properties of reversible Zn electrodeposition. This strategy enables us to design electrolytes with 99% Coulombic efficiency that support reversible optical contrast on electrodes. X-ray diffraction and scanning electron microscopy analyses establish connections between the composition and morphology of the electrodeposits and the composition of the electrolytes. Although electrode degradation and H_2 evolution are thermodynamically favorable under the operating voltages of the electrolytes due to the negative standard reduction potential of Zn/Zn^{2+}, we find that these reactions are kinetically passivated by the Zn and ZnO electrodeposits. An understanding of these electrochemical properties allows us to construct 25 cm^2 dynamic windows that switch with 64% optical contrast at 600 nm within 30 s. Because we utilize non-noble Zn as opposed to the noble metals commonly used in previous electrolytes, this work expands the chemical scope of electrolytes in dynamic windows based on reversible metal electrodeposition, which should lead to future advances in electrolyte design.

Introduction

One important method of reducing energy consumption is to increase the energy efficiency of buildings, which are responsible for about half of the electricity consumed in the United States.[1] A promising way of increasing building energy efficiency is to decrease lightning, heating, and cooling consumption by implementing dynamic windows with electronically tunable transmission. The replacement of energy-efficient low-emissivity static windows with dynamic windows leads to an average of 10% energy savings in buildings.[2, 3]

Devices containing electrochromic materials are the most common form of dynamic windows and have existed for decades.[4-7] Electrochromics refer to any material that change their optical properties upon application of a voltage and include transition metal oxides, polymers, small molecules, and nanoparticles.[8] Electrochromic windows can possess high optical contrasts, long cycle lives, and fast switching speeds.[9-11] However, many electrochromic devices do not possess all of these attributes along with the low production costs needed for widespread adoption. In addition to electrochromic materials, polymer dispersed liquid crystals (PDLCs) are also commonly used to construct dynamic windows.[12] Although PDLC devices possess millisecond switching times, they transition between a clear state and a bright hazy state, which is undesirable for many applications in which maintaining image fidelity is important.[13] Thermochromic windows, which turn opaque upon solar heating, have also been investigated for decades, but these windows switch passively, and thus do not provide users with control over their transparency.[14, 15] Thus, all of these approaches have drawbacks, and the ideal set of attributes for a dynamic window has not been achieved yet through a single technology.

Reversible metal electrodeposition for dynamic windows is a burgeoning technology that is a promising alternative to electrochromics, PDLCs, and thermochromics.[16] Metals are promising

materials for light modulation in dynamic windows due to several intrinsic properties. Most metals are chemically inert, color neutral, photostable, and highly opaque in their elemental form.[17, 18] An additional benefit is that many dynamic windows based on reversible metal electrodeposition can be constructed through inexpensive solution processing.[19, 20]

Metal-based dynamic windows consist of a transparent conducting working electrode such as tin-doped indium oxide (ITO), a counter electrode, and a gel or liquid electrolyte containing salts of colorless metal ions.[21] Upon applying a reductive potential to the working electrode, the metal ions in the electrolyte are reduced to elemental metal on the transparent conductor to turn the device dark. At the same time, oxidation occurs at the counter electrode to charge balance this reaction. In some embodiments, oxidation of a metal counter electrode frame or a transparent metal mesh occurs.[22-24] In other devices, the counter electrode facilitates intercalation chemistry through the oxidation of a transparent thin film host material such as NiO or a hexacyanoferrate.[25-27]

Previous dynamic windows harnessing reversible metal electrodeposition have relied upon the electrodeposition of Ag, Pb, Cu, Bi, and Au.[28-32] Each of these metals has its own advantages and disadvantages. Among the most successful dynamic windows have been those based on the coelectrodeposition of Bi and Cu.[24, 33] However, Bi-based electrolytes possess limited ion solubility due to the proclivity to form insoluble $Bi(OH)_3$ under aqueous conditions.[18] All of the metals used in these windows are relatively noble. Indeed, the focus on utilizing noble metals has been a guiding principle in the development of these devices.[16, 31] This principle stems from the fact that in aqueous electrolytes, the evolution of hydrogen must be avoided. The more noble the metal electrodeposited, the less thermodynamically favorable it is to generate hydrogen during device operation. For this reason, non-noble metals are not commonly explored for metal-based dynamic windows.

In this manuscript, we broaden the paradigm for which metals can be used in reversible metal electrodeposition electrolytes for dynamic windows by demonstrating fully functional Zn electrolytes. Despite the fact that Zn is a non-noble metal with a standard reduction potential of -0.76 V vs. NHE,[34] we demonstrate that the hydrogen evolution reaction and other deleterious side reactions can be kinetically passivated in properly designed reversible Zn electrodeposition electrolytes. These Zn electrolytes possess high Coulombic efficiency and support the formation of a highly opaque metal film. In addition to probing the fundamental electrochemical properties of these electrolytes, their successful design allows us to construct practical two-electrode dynamic windows that possess high optical contrast. Although a recent publication utilized reversible Zn electrodeposition on a metal grid as a counter electrode,[35] to the best of our knowledge, this work is the first to use reversible Zn electrodeposition on a transparent conducting oxide working electrode. By harnessing a non-noble metal, this work diversifies the chemical space of reversible metal electrodeposition on transparent conductors.

Experimental

Chemicals were received from commercial sources and used without further purification. Half-cell experiments were performed using a Zn metal (A Metal Source, LLC, 99.9%) reference electrode, a separate Zn metal counter electrode, and a Pt-modified ITO on glass working electrode with a geometric surface area of 3 cm^2. Electrochemistry was conducted using a VSP-300 Biologic potentiostat. All CV data presented is the second cycle unless otherwise stated. Transmission data were recorded with an Ocean Optics FLAME-S-VIS-NIR spectrometer together with an Ocean Optics DH-mini UV-Vis-NIR light source.

Various electrolytes were studied with their compositions listed in the figure captions. $ZnCl_2$ (98%), $ZnBr_2$ (98%), ZnI_2 (99%), sodium formate (98%), sodium acetate (99%), sodium

chloroacetate (98%), sodium trichloroacetate (97%), sodium trifluoroacetate (98%), and sodium chlorodifluoroacetate (96%) were purchased from Oakwood Chemicals. Sodium propionate (99%) and sodium butyrate (98%) were purchased from Sigma Aldrich. Solutions were prepared by adding the appropriate solids to 20 mL of de-ionized water. The pH values of the solutions were then adjusted to 4.8 ± 0.3 with the conjugate acid of an electrolyte anion. The solutions were next converted to gels by the addition of 2% wt. hydroxyethylcellulose (Sigma Aldrich, average M_v ~90,000) and overnight stirring.

Pt-modified ITO on glass electrodes were prepared by spray coating a 3:1 mixture of water:Pt nanoparticles (Sigma Aldrich, 3 nm in diameter) on ITO on glass substrates (Xinyan Technology, 15 Ω sq^{-1}). The Pt-modified ITO on glass substrates were then heated under air at 250°C for 20 minutes.

For two-electrode 25 cm^2 dynamic windows, Cu tape with conductive adhesive (TapesMaster.com) was first placed along the edges of the Pt-modified ITO on glass to make uniform electrical connection to the working electrode. The counter electrode was comprised of Zn foil placed on top a nonconductive glass backing. Butyl rubber (ZXMT, Ltd.) was placed around the edges of the device stack to seal the two electrodes together with an interelectrode spacing of ~5 mm. The gel electrolyte was then injected into the device stack through the butyl rubber sealant via a syringe. The outside surfaces of the completed dynamic window were cleaned with glass cleaner before performing the optical measurements.

Scanning electron microscope (SEM) images were obtained using a JOEL JSM-6010LA microscope with an operating voltage of 20 kV. X-ray diffraction (XRD) was conducted using a Bruker D2 X-ray Diffractometer. To estimate the relative percentages of Zn and ZnO, the integral of the XRD peaks for Zn located at ~39° and ~43° were compared to the integral of the peak for

ZnO located at ~36°. The Zn/ZnO electrodeposits for SEM and XRD analysis were formed by conducting linear sweep voltammograms at a scan rate of 5 mV s^{-1} from 0 V to -1 V.

Results and Discussion

Zn Haloacetate Electrolytes

As a starting point for designing reversible Zn electrodeposition electrolytes, we used an electrolyte containing 0.5 M $ZnCl_2$ and 0.5 M $NaCH_3COO$. This composition using relatively simple salts is inspired in part by a previous electrolyte containing $ZnSO_4$ and KCl used in dynamic windows that facilitate reversible Zn electrodeposition on a stainless steel mesh.[35] The acetate-chloride electrolyte evaluated here supports electrochemically (Figure 1, black line) and optically reversible Zn electrodeposition. On a Pt-modified ITO working electrode, an electrode commonly used to enhance metal nucleation in reversible metal electrodeposition devices,[23] cyclic voltammetry (CV) shows that Zn electrodeposition commences at about -30 mV vs. Zn/Zn^{2+}. This onset potential, which is close to 0 V, indicates that Zn electrodeposition has a low overpotential in this electrolyte. After electrodeposition occurs, the positive current at voltages greater than 0 V is due to the oxidization of Zn off of the electrode to form Zn^{2+}. The rapid decrease in the current after the anodic peak around 1.3 V is due to the complete depletion of Zn from the electrode. The Coulombic efficiency, as defined by the ratio of the integrated anodic charge to the integrated cathodic charge in the CV, for this electrolyte is 98%, indicating good electrochemical reversibility.

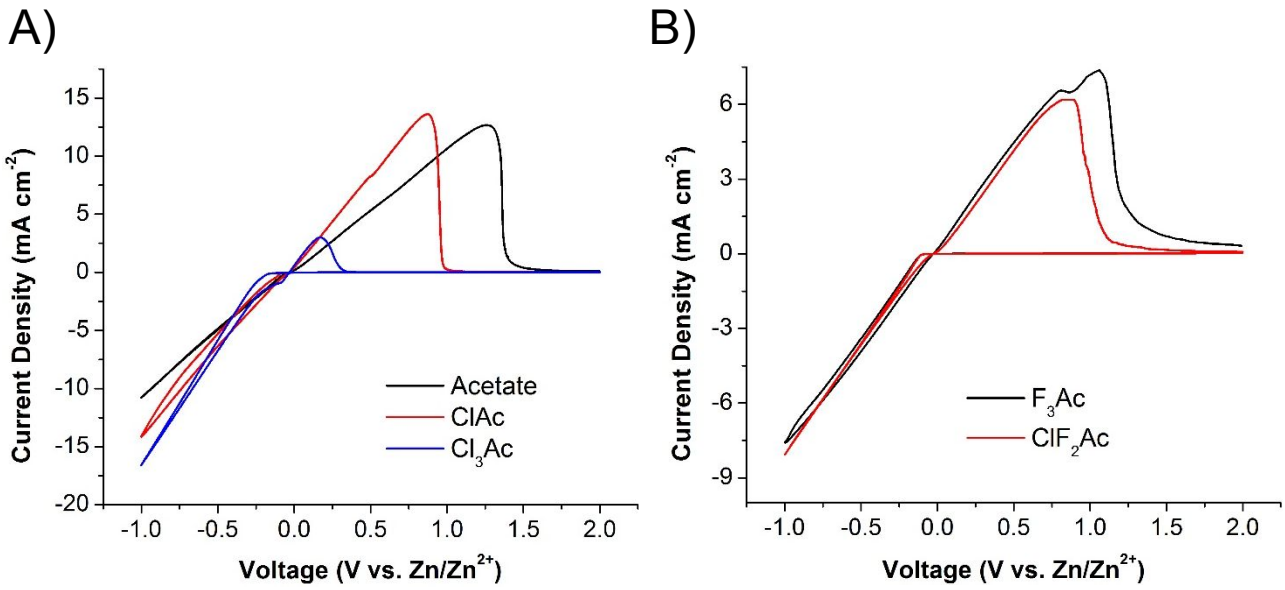

Figure 1: Cyclic voltammograms at a scan rate of 25 mV s^{-1} of Pt-modified ITO working electrodes in electrolytes containing 0.5 M $ZnCl_2$ and 0.5 M $NaCH_3COO$ (sodium acetate, panel A, black line), $NaCClH_2COO$ (sodium chloroacetate, ClAc, panel A, red line), $NaCCl_3COO$ (sodium trichloroacetate, Cl_3Ac, panel a, blue line), $NaFCH_2COO$ (sodium fluoroacetate, panel B, black line), or $NaClF_2COO$ (sodium chlorodifluoroacetate, panel B, red line).

In an effort to understand the electrochemical behavior of this electrolyte, we systematically altered the chemical identity of its acetate component. First, we evaluated the electrochemistry of Zn electrolytes with halogen-substituted acetates. Substituting one of the hydrogen atoms of acetate with chlorine gives chloroacetate. Although the Zn electrolyte with chloroacetate possesses the same general Zn deposition and stripping features as the acetate electrolyte, there are important differences. First, the onset potential for Zn deposition is about -70 mV, a value that is 40 mV more negative than that of the acetate electrolyte. Second, the Coulombic efficiency obtained from the CV with the chloroacetate electrolyte is 60% as compared to the 98% value in the acetate electrolyte (Figure 2A). These findings indicate that both the Zn deposition and stripping processes are impeded with chloroacetate relative to acetate.

The complete chlorine substitution of acetate in a trichloroacetate electrolyte further inhibits the Zn deposition and stripping reactions. The onset potential for Zn deposition in the

trichloroacetate electrolyte shifts further negative to -150 mV, indicating that there is a significant kinetic barrier for Zn deposition to occur using this electrolyte. Additionally, the Coulombic efficiency of the trichloroacetate CV further decreases to only 4% (Figure 2A), which signifies that the Zn stripping reaction is slow in the presence of trichloroacetate. Taken together, these results indicate that chlorine substitution on the acetate ligand decreases the kinetics of reversible Zn electrodeposition.

We next evaluated electrolytes with fluorine-substituted acetates. Figure 1B displays CVs of reversible Zn electrodeposition in electrolytes containing trifluoroacetate and chlorodifluoroacetate. Like the trichloroacetate electrolyte, these two electrolytes contain trihaloacetates. However, the Coulombic efficiencies of the two CVs are significantly higher than that of the trichloroacetate CV (Figure 2A). In particular, the trifluoroacetate CV possesses a higher Coulombic efficiency than the chlorodifluoroacetate CV, indicating that a greater number of fluorine substitutions enhances Zn stripping kinetics.

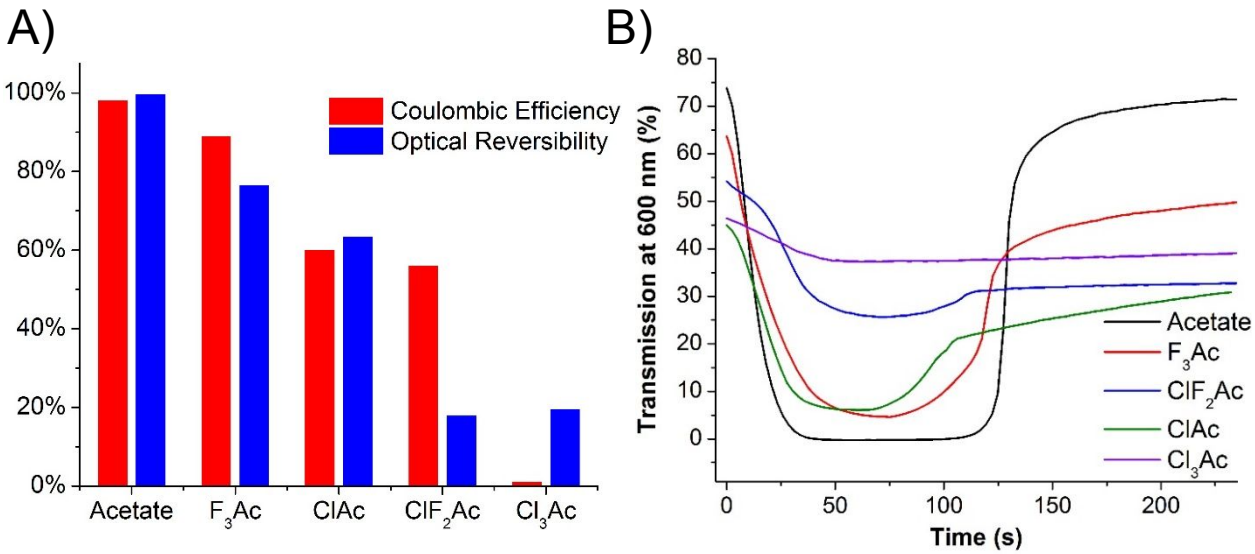

Figure 2: Coulombic efficiency and optical reversibility for Zn electrolytes containing different -acetates (A) along with the transmission at 600 nm of the working electrode during the second cycle of CVs in these electrolytes (B). The corresponding CVs are displayed in Figure 1.

Figure 2B displays the transmission at 600 nm of the working electrodes during one CV cycle of reversible Zn electrodeposition in the various acetate electrolytes as measured in a spectroelectrochemical cell. For the electrolyte containing unsubstituted acetate, the transmission begins at about 74% and decreases to nearly 0% during metal electrodeposition (Figure 2B, black line). During the stripping portion of the CV, the transmission returns close to its original 74% value, indicating that reversible Zn electrodeposition from this acetate electrolyte is nearly completely optically reversible under these conditions. The optical reversibility of the electrode during the CV cycle is defined as the ratio of the transmission changes during the deposition and stripping processes, and is given by Equation 1, where $T_{initial}$ is the transmission at the beginning of the CV, T_{final} is the transmission at the end of the CV, and T_{min} is the minimum transmission recorded during the CV.

$$Optical\ Reversibility = \frac{T_{final} - T_{min}}{T_{initial} - T_{min}} \quad \text{(Equation 1)}$$

Electrodes using electrolytes with halide-substituted acetates do not get nearly as opaque as the electrode using the unsubstituted acetate electrolyte. Furthermore, the electrolytes with substituted acetates all possess optical reversibilities less than 100%. The lack of optical reversibility in these electrolytes correlates well with their decreased Coulombic efficiencies (Figure 2A), which is indicative of slower stripping kinetics. We note that in Figure 2B, the starting transmission values of all of the electrolytes differ substantially. These differences arise from the fact that the data analyzed were taken from the second CV cycles, and so optical irreversibility in the first CV cycle resulted in a decreased initial transmission value for the substituted acetate electrolytes. We chose to analyze the second cycle of the CVs because initial nucleation processes occur on the ITO working electrode during the first CV cycle that complicate analysis.[19]

Effects of Ligand Chain Length on Zn Electrolytes

In addition to studying the effect of haloacetates, we also investigated electrolytes containing $ZnCl_2$ and various chain lengths of carboxylates. Figure 3 displays CVs of the Zn electrolytes with formate, propionate, or butyrate in place of acetate. All three CVs exhibit the typical features associated with Zn electrodeposition and stripping. However, a clear trend emerges when analyzing the Coulombic efficiencies of the CVs, which increase using carboxylates with shorter chain lengths (Figure 4A, red bars). In particular, the CV for the formate electrolyte possesses a Coulombic efficiency of 99% as compared to 98% for the acetate electrolyte, indicating that Zn stripping kinetics are accelerated with the formate anion.

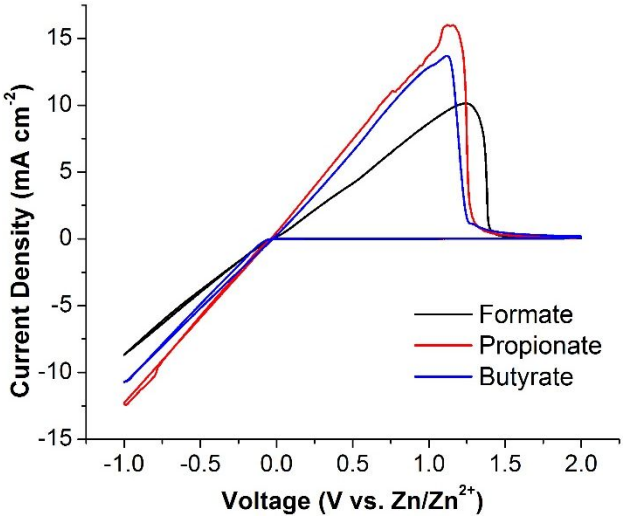

Figure 3: Cyclic voltammograms at a scan rate of 25 mV s^{-1} of Pt-modified ITO working electrodes in electrolytes containing 0.5 M $ZnCl_2$ and 0.5 M sodium formate (black line), sodium propionate (red line), or sodium butyrate (blue line).

As for the haloacetate electrolytes, the trend in the optical reversibilities of the electrolytes with different carboxylates also follows the Coulombic efficiency trend (Figures 2A and Figure 4A). In particular, the transmission of the working electrode when using the formate electrolyte returns back to its original ~77% value after the stripping portion of the CV is completed, indicating that this electrolyte exhibits complete optical reversibility (Figure 4B, black line).

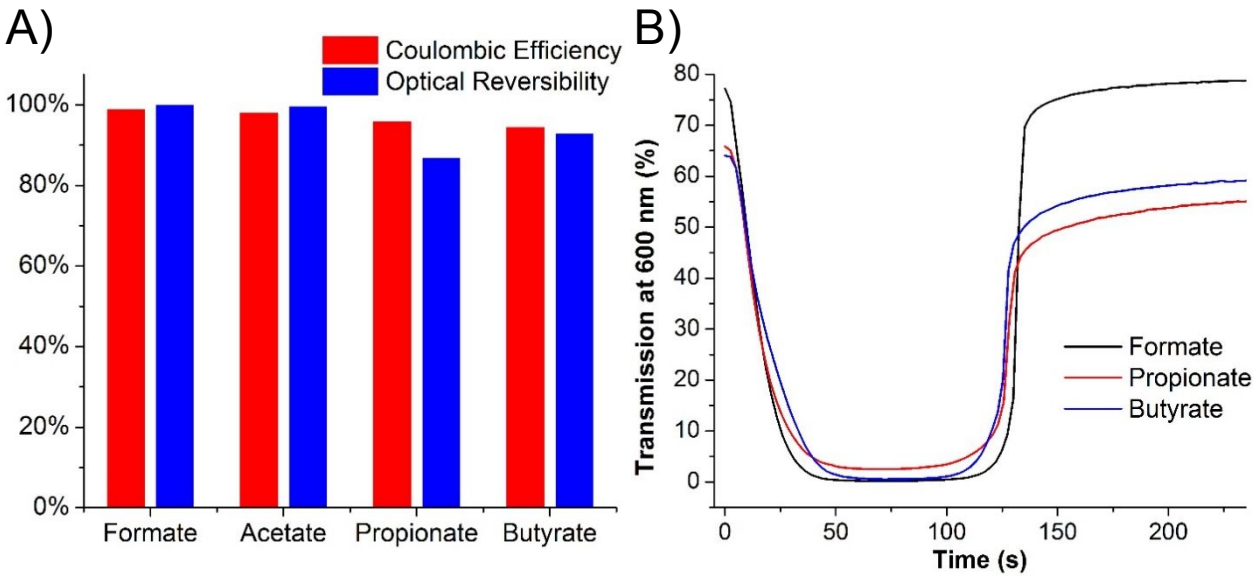

Figure 4: Coulombic efficiency and optical reversibility for Zn electrolytes containing different chain lengths of carboxylates (A) along with the transmission at 600 nm of the working electrode during the second cycle of CVs in these electrolytes (B). The corresponding CVs are displayed in Figure 3.

Effect of Halides on Zn Electrolytes

We next studied the effect of halide compositions on the Zn electrolytes. Because in the section above, we found that both the acetate and formate electrolytes possess good Coulombic efficiency and optical reversibility, we investigated the influence of halide composition on both of these systems with a particular focus on the formate electrolytes due to their enhanced stripping kinetics.

Figure 5A displays CVs of Zn electrodeposition and stripping in formate electrolytes with $ZnCl_2$, $ZnBr_2$, and a 1:1 mixture of $ZnCl_2$ and $ZnBr_2$. The CV of the electrolyte containing $ZnBr_2$ (red line) possesses approximately twice the deposition current as the CV of the $ZnCl_2$ electrolyte (black line), and as a result, the $ZnBr_2$ CV also exhibits about twice as much stripping current. In Cu electrodeposition baths, the bromide anion is known to be an accelerant for electrodeposition that operates via the formation of bridging halide complexes,[36, 37] and a similar phenomenon may explain the enhanced deposition current observed with the $ZnBr_2$ electrolyte. However, because

bromide induces morphological differences in Zn electrodeposits, the $ZnBr_2$ electrolyte results in films that switch to their opaque states as quickly as those formed using $ZnCl_2$ (*vide infra*) despite the increased current sustained by the $ZnBr_2$ electrolyte. For this reason, we also studied a 1:1 mixture of $ZnCl_2$ and $ZnBr_2$ with the intention of accelerating deposition kinetics while maintaining an optically favorable electrodeposit morphology. Interestingly, the CV of the $ZnCl_2$-$ZnBr_2$ electrolyte (blue line) possesses similar currents as the CV of the $ZnCl_2$ electrolyte (black line). This result suggests that the $ZnCl_2$-$ZnBr_2$ electrolyte is dominated by chlorine species from which electrodeposition occurs. Indeed, Zn-Cl bonds are significantly stronger than Zn-Br bonds, which explains the greater stability of Zn-Cl electrodeposition precursors.[38]

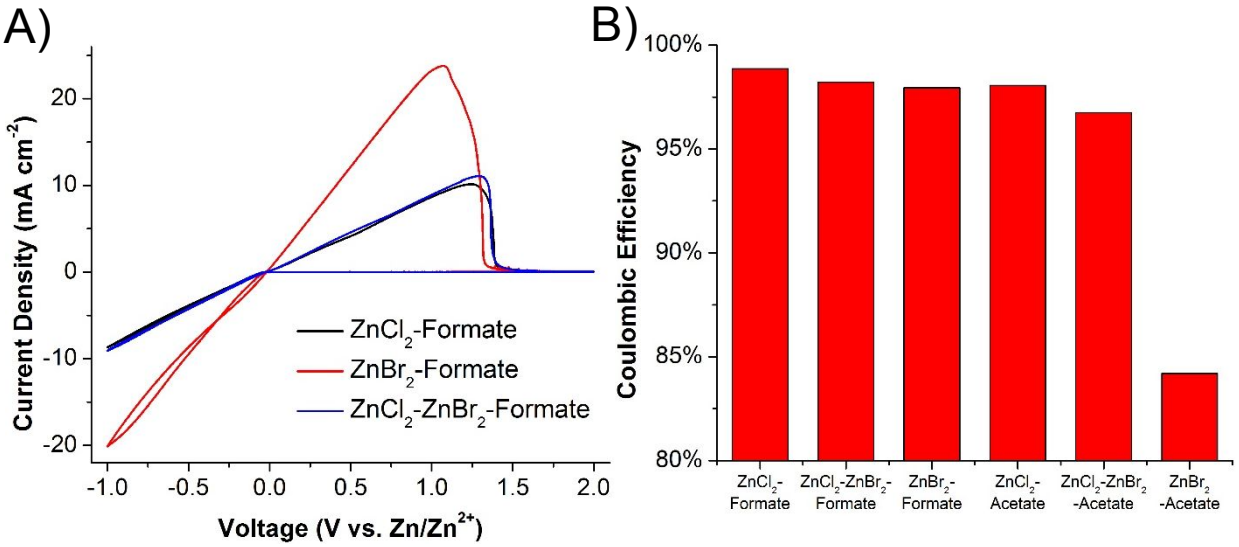

Figure 5: Cyclic voltammograms (A) at a scan rate of 25 mV s^{-1} of Pt-modified ITO working electrodes in electrolytes containing 0.5 M sodium formate and 0.5 M $ZnCl_2$ (black line), 0.5 M $ZnBr_2$ (red line), or 0.25 M $ZnCl_2$ and 0.25 M $ZnBr_2$ (blue line). Coulombic efficiencies (B) of the CVs of formate and acetate electrolytes with various halide compositions.

The Coulombic efficiencies of the CVs increase in the order of $ZnCl_2$ > $ZnCl_2$-$ZnBr_2$ > $ZnBr_2$ for both the formate and acetate electrolytes (Figures 5B and S1). Furthermore, for a given halide composition, each formate electrolyte exhibits a higher Coulombic efficiency than the corresponding acetate electrolyte due to the enhanced stripping kinetics of formate as discussed previously. We hypothesize that the greater Coulombic efficiencies in the electrolytes containing

$ZnCl_2$ is due to enhanced stripping kinetics of chloride that result from the greater stability of Zn-Cl coordination complexes.

We also tested an electrolyte containing ZnI_2. The iodide-containing electrolyte produced a yellow-colored solution as a result of the oxidation of iodide to iodine during the anodic portion of the CV (Figure S2). This iodine formation interfered with measurements of the transmission of the working electrode (Figure S3), and thus ZnI_2 electrolytes were not studied further. ZnF_2 electrolytes could not be examined due to the insolubility of ZnF_2 in water.

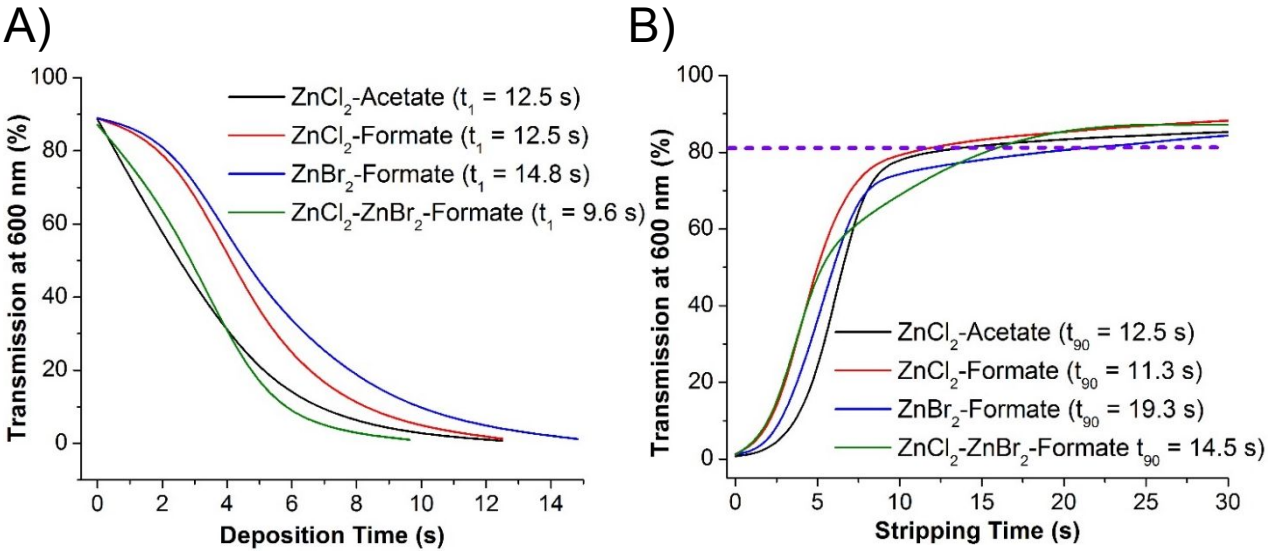

Figure 6: Transmission at 600 nm of the working electrode during Zn electrodeposition (A) and stripping (B) in electrolytes containing 0.5 M sodium acetate and 0.5 M $ZnCl_2$ (black line), or 0.5 M sodium formate and 0.5 M $ZnCl_2$ (red line), 0.5 M $ZnBr_2$ (blue line), or 0.25 M $ZnCl_2$ and 0.25 M $ZnBr_2$ (green line). To elicit Zn electrodeposition, chronoamperometry was conducted at -1.0 V until the transmission at 600 nm reached 1%. Next, Zn stripping was conducted at +2.5 V for 30 s.

Given the high Coulombic efficiencies (≥ 98%) of the $ZnCl_2$-acetate, $ZnCl_2$-formate, $ZnBr_2$-formate, and $ZnCl_2$-$ZnBr_2$-formate systems, we studied these four electrolytes using chronoamperometry to better assess their deposition and stripping speeds (Figure S4). Figure 6 displays the transmission of the working electrode at 600 nm during Zn electrodeposition and

stripping. Electrodeposition was elicited by applying a potential of -1.0 V until the transmission reached 1% (Figure 6A). Upon reaching 1% transmission, the potential was switched to +2.5 V to induce metal stripping (Figure 6B). This procedure allows for the comparison of electrode darkening and lightening speeds at a fixed contrast ratio (i.e. switching between a 88% clear state to a 1% dark state) among the four electrolytes. The stripping voltage of +2.5 V is much higher than the +0.8 V our group previously used for Bi-Cu dynamic windows.[20] To facilitate fast stripping, it is advantageous to apply as oxidizing of a stripping voltage as possible that does not result in adverse side reactions. Because the standard reduction potential of Zn^{2+}/Zn is about 1.1 V more negative than those of Bi^{3+}/Bi and Cu^{2+}/Cu,[34] +2.5 V vs. Zn^{2+}/Zn is equivalent to +1.4 V vs. Bi and Cu. Despite the fact that the Zn stripping voltage used here is still about +0.6 V more oxidizing than the +0.8 V used in the Bi-Cu devices, no adverse side reactions were witnessed during stripping.

For both the $ZnCl_2$-acetate and $ZnCl_2$-formate electrolytes, the time it takes to reach 1% transmission is 12.5 s (Figure 6A, black and red lines). However, the darkening speed decreases to 14.8 s with the $ZnBr_2$-formate electrolyte (Figure 6A, blue line) despite the additional deposition current observed with $ZnBr_2$ (Figure 5A). This finding implies that the morphology of the Zn electrodeposits with the $ZnBr_2$ electrolyte are less effective at blocking light than the $ZnCl_2$ electrolyte. This supposition is confirmed by SEM analysis (*vide infra*). Strikingly, the fastest darkening speed of 9.6 s is obtained with the $ZnCl_2$-$ZnBr_2$-formate electrolyte. The interpretation of this result is discussed later in the manuscript.

Electrode lightening speeds were assessed by calculating the time it takes the electrode to complete 90% of its transmission change during metal stripping (t_{90} values, dashed purple line, Figure 6B). The t_{90} value for the $ZnCl_2$-formate electrolyte (11.3 s) is less than for the $ZnCl_2$-

acetate electrolyte (12.5 s) due to the enhanced stripping kinetics by the less sterically bulky formate anion as discussed previously. The lightening speeds for the three formate electrolytes increase in the order of $ZnCl_2$ > $ZnCl_2$-$ZnBr_2$ > $ZnBr_2$. This trend directly correlates with the same order of increasing Coulombic efficiency (Figure 5B), which demonstrates the enhanced stripping kinetics imparted by chloride.

Surface Characterization of Zn Electrodeposits

To investigate the morphology of the Zn electrodeposits as a function of halide composition in the electrolyte, we use SEM to image the electrodeposits. The Zn electrodeposits obtained from the $ZnCl_2$ (Figures 7A and 7B) and $ZnCl_2$-$ZnBr_2$ (Figure 7E and 7F) electrolytes are relatively similar and consist of a uniform film of material decorated with protrusions approximately 1 μm in length. In contrast, the morphology of the electrodeposits obtained from the $ZnBr_2$ electrolyte is markedly different and consists of a lower density of larger particles (>10 μm in length) with visible gaps in between them. These images suggest that in the $ZnBr_2$ electrolyte, the metal nucleation density is lower than in the chloride-containing electrolytes, which gives rise to more nonuniform growth. Larger particles, however, grow in the $ZnBr_2$ electrolyte because of the enhanced deposition kinetics observed with bromide as discussed previously. These larger and less uniform particles that contain gaps are less effective at blocking light compared to the more uniformly distributed electrodeposits obtained from the chloride-containing electrolytes. These results explain why the $ZnBr_2$-formate electrolyte exhibits a slower darkening time as compared to the $ZnCl_2$-formate and $ZnCl_2$-$ZnBr_2$-formate electrolytes (Figure 6A) despite the greater magnitude of current measured during the CVs (Figure 5A). SEM images of electrodeposits grown using the $ZnCl_2$-$ZnBr_2$-formate electrolyte were also obtained after halting the voltammetry at different voltages (Figure S5).

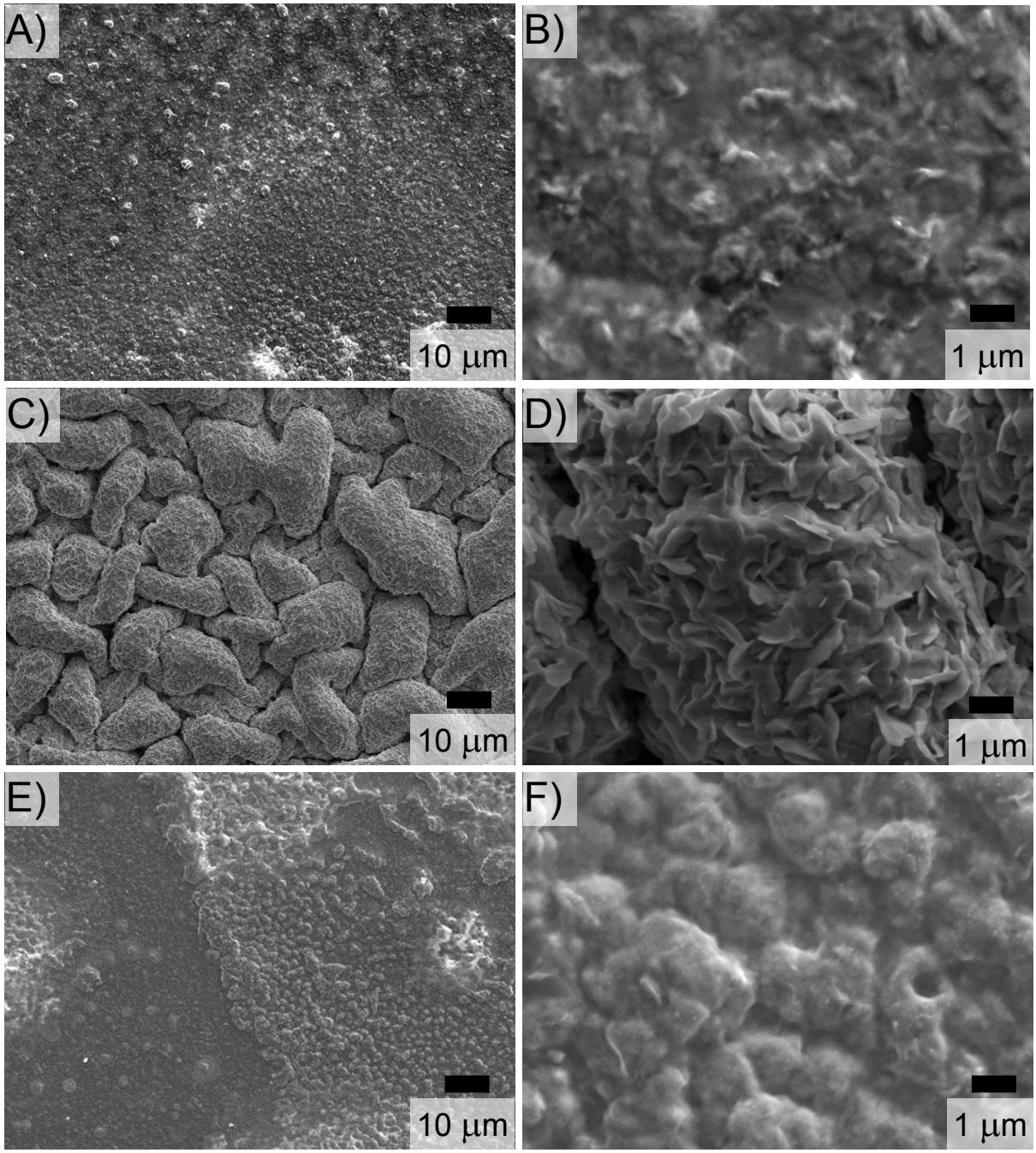

Figure 7: Scanning electron microscopy images of Zn electrodeposits obtained after a linear sweep voltammogram from 0 V to -1 V at 5 mV s^{-1} in an electrolyte containing 0.5 M sodium formate and 0.5 M $ZnCl_2$ (A, B), 0.5 M $ZnBr_2$ (C, D), or 0.25 M $ZnCl_2$ and 0.25 M $ZnBr_2$ (E, F). The transmissions at 600 nm of the electrodes were 1%.

However, given the fairly similar morphologies of the electrodeposits obtained from the $ZnCl_2$ and $ZnCl_2$-$ZnBr_2$ electrolytes, it is unclear at this stage of our analysis why the $ZnCl_2$-$ZnBr_2$ electrolyte possesses a faster darkening speed (Figure 6A). To complement the SEM

morphological data, we used XRD to probe the chemical composition of the electrodeposits. XRD analysis shows that the electrodeposits consist predominantly of Zn and ZnO (Figure S6). By comparing the ratios of the integrated peaks in the XRD spectra for Zn and ZnO, we were able to gauge the oxide content in the various electrodeposits (Figure 8).

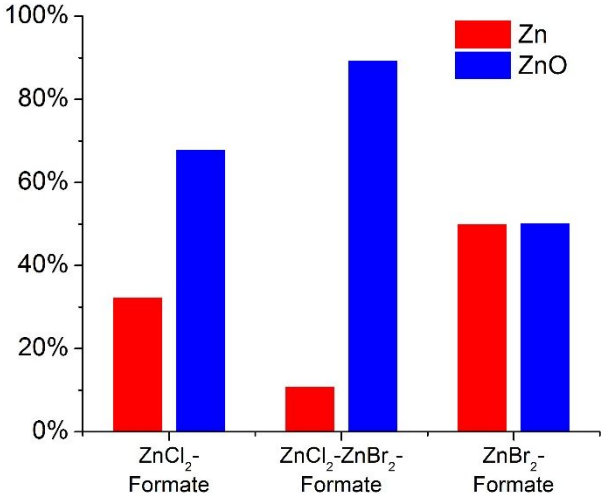

Figure 8: Relative compositions of Zn and ZnO as determined by X-ray diffraction of Zn electrodeposits obtained using the conditions described in Figure 7.

Interestingly, electrodeposits obtained from the $ZnCl_2$-$ZnBr_2$ electrolyte have a significantly higher percentage of ZnO than electrodeposits created from the $ZnCl_2$ or $ZnBr_2$ systems. Perhaps the greater quantity of ZnO causes the electrodeposits formed from the $ZnCl_2$-$ZnBr_2$ electrolytes to block light more effectively than the morphologically-similar electrodeposits obtained from $ZnCl_2$. However, because the extinction coefficient of ZnO is substantially less than Zn,[39, 40] uniform thin films of pure ZnO block less light than a uniform Zn film of the same thickness. This inconsistency means that a completely uniform thin film of Zn or ZnO is an inadequate way of modeling the optics of these electrodeposits. It is likely that more complex optical phenomena occur within the electrodeposits, which are highly heterogeneous both in terms of their physical and chemical structures.

The Electrochemical Window of ITO in Zn Electrodeposition Electrolytes

As mentioned in the introduction, dynamic windows based on reversible metal electrodeposition typically harness relatively noble metals such as Cu, Bi, and Ag.[16] These metals have standard reduction potentials more positive than H_2, and therefore, it is thermodynamically more favorable in aqueous electrolytes to electrodeposit these metals as opposed to generating H_2, which is not tolerable for window applications.[34] Not only is there the potential issue of H_2 generation with less noble metals, electrodepositing metals with more negative reduction potentials can also lead to the application of voltages outside of the electrochemical window of transparent conductors like ITO. For instance, ITO is known to degrade at voltages more negative than about -0.3 V vs. Zn^{2+}/Zn at neutral pH.[41]

Despite the instability of ITO and the thermodynamic possibility of H_2 generation at negative potentials, we do not observe ITO degradation or H_2 generation in any of the studied Zn electrolytes when cycling between +2.0 V and -1.0 V vs. Zn^{2+}/Zn. These findings suggest that some property of the Zn electrolytes impedes H_2 evolution and ITO degradation, thus protecting the electrode from undergoing these unwanted side reactions.

We performed a series of CV experiments to interrogate how the Zn electrolytes protect the ITO electrode and prevent H_2 formation. These experiments have three distinct stages. In the first stage, we conducted a CV in the previously described electrolyte containing sodium formate, $ZnCl_2$, and $ZnBr_2$ (Figure 9A, black line). During the second cycle of this CV, the experiment was stopped at -0.1 V during the negative going sweep (E_{final} = -0.1 V). As a result, the working electrode at this stage contained a small amount of electrodeposited Zn on its surface.

In the second stage of the experiment, the electrode was removed from the first electrolyte and placed in a second electrolyte containing sodium formate without any Zn salts. The CV in this

blank formate electrolyte still contains the characteristic reversible Zn deposition and stripping peaks (Figure 9A, red line). These peaks are due to the stripping and redepositing of Zn that was originally electrodeposited during the first stage. (In part, the peaks are also due to Zn^{2+} impurities in the blank electrolyte, which come from residual Zn electrolyte on the original wet electrode. We do not rinse the electrode before moving it to the blank formate electrolyte so as to not destroy the integrity of the electrodeposited Zn film.)

Finally, in the third stage of the experiment, the electrode is removed from the second electrolyte and placed in a third electrolyte, which is a freshly prepared solution containing sodium formate, $ZnCl_2$, and $ZnBr_2$. The CV of the electrode in this new $ZnCl_2$-$ZnBr_2$-formate electrolyte (Figure 9A, blue line) is similar to the CV of the electrode in the first electrolyte (Figure 9A, black line). The similarity of the CVs before and after cycling in the blank formate electrolyte indicates that cycling in the blank formate electrolyte does not degrade the ITO electrode when E_{final} = -0.1 V.

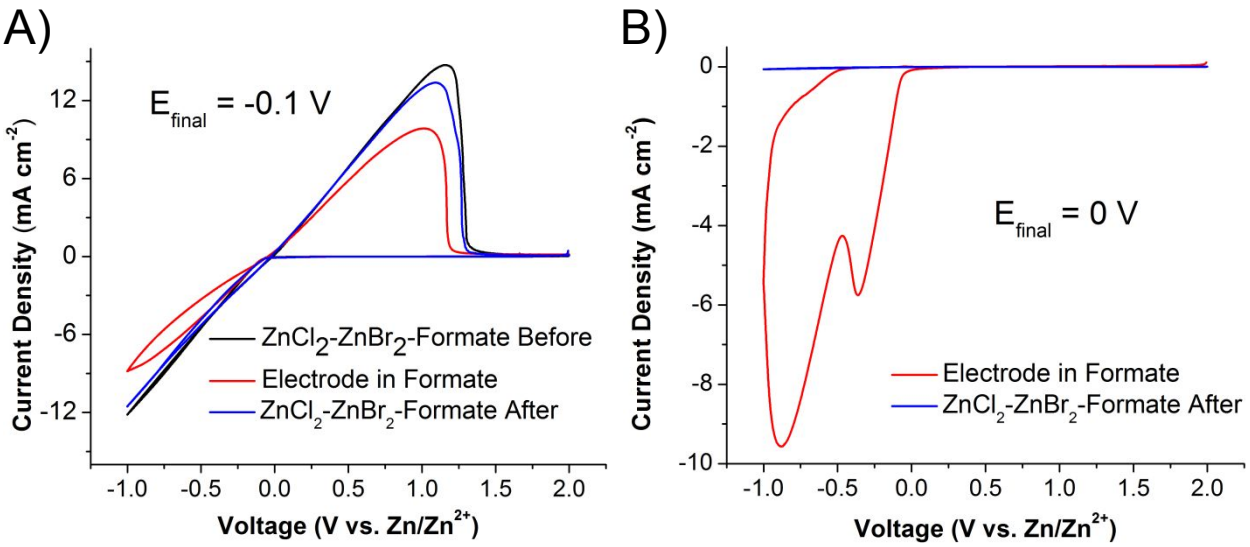

Figure 9: Cyclic voltammogram obtained using the $ZnCl_2$-$ZnBr_2$-formate electrolyte containing 0.5 M sodium formate, 0.25 M $ZnCl_2$, and 0.25 M $ZnBr_2$ (A, black line). The experiment was halted at -0.1 V (E_{final}) during the negative sweep of the second cycle. After obtaining this voltammogram, the same working electrode was used in an electrolyte containing only 0.5 M sodium formate (A, red line). Lastly, the same working electrode was used a second time in the $ZnCl_2$-$ZnBr_2$-formate electrolyte (A, blue line). For panel B, a fresh working electrode was also

first cycled in the $ZnCl_2$-$ZnBr_2$-formate electrolyte. The experiment was halted at an E_{final} = 0 V during the negative sweep of the second cycle. After obtaining this voltammogram, the same working electrode was used in an electrolyte containing only 0.5 M sodium formate (B, red line). Lastly, the same working electrode was used a second time in the $ZnCl_2$-$ZnBr_2$-formate electrolyte (B, blue line).

With a new working electrode, we next performed the same three-part experiment, but during the first CV in the $ZnCl_2$-$ZnBr_2$-formate electrolyte, the negative going sweep was halted at 0 V during the second cycle (E_{final} = 0 V). Because the experiment was halted before Zn electrodeposition occurred during the second cycle, the electrode did not contain a significant amount of Zn at this stage. Next, the electrode was placed in the blank formate electrolyte. The CV in the blank formate electrolyte does not contain the typical Zn electrodeposition and stripping peaks (Figure 9B, red line). Instead, the cathodic peaks observed are a combination of H_2 evolution and ITO degradation to metallic In and Sn. In the third stage of the experiment, the electrode was placed back in the $ZnCl_2$-$ZnBr_2$-formate electrolyte. Notably, the CV in this case shows little current density throughout the scan (Figure 9B, blue line). This result indicates that the ITO electrode degraded and as such no longer supports reversible Zn electrodeposition.

In summary, H_2 evolution and ITO degradation occur when E_{final} = 0 V, but not when E_{final} = -0.1 V. These results demonstrate that Zn electrodeposits protect the ITO electrode from degradation and from evolving H_2. During the second stage of the experiments in the blank formate electrolyte, the Zn electrodeposits are only present on the electrode when E_{final} = -0.1 V. It is known that Zn is a poor catalyst for the H_2 evolution reaction,[42] and in this way the electrodeposited Zn prevents the system from generating H_2 even at relatively high magnitude cathodic potentials. Furthermore, the Zn electrodeposits protect the ITO from degrading into metallic In and Sn likely by physically blocking access of the electrolyte to the ITO surface. In this manner, the

electrochemical window of ITO is expanded in the presence of reversible Zn electrodeposition electrolytes.

Practical Two-Electrode Devices using Reversible Zn Electrodeposition

Having designed and investigated reversible Zn electrodeposition electrolytes, we next constructed practical two-electrode 25 cm^2 dynamic windows using these electrolytes. We built these windows with the electrolyte containing $ZnCl_2$, $ZnBr_2$, and sodium formate because our studies described above determined that this electrolyte has a high Coulombic efficiency and fast switching times.

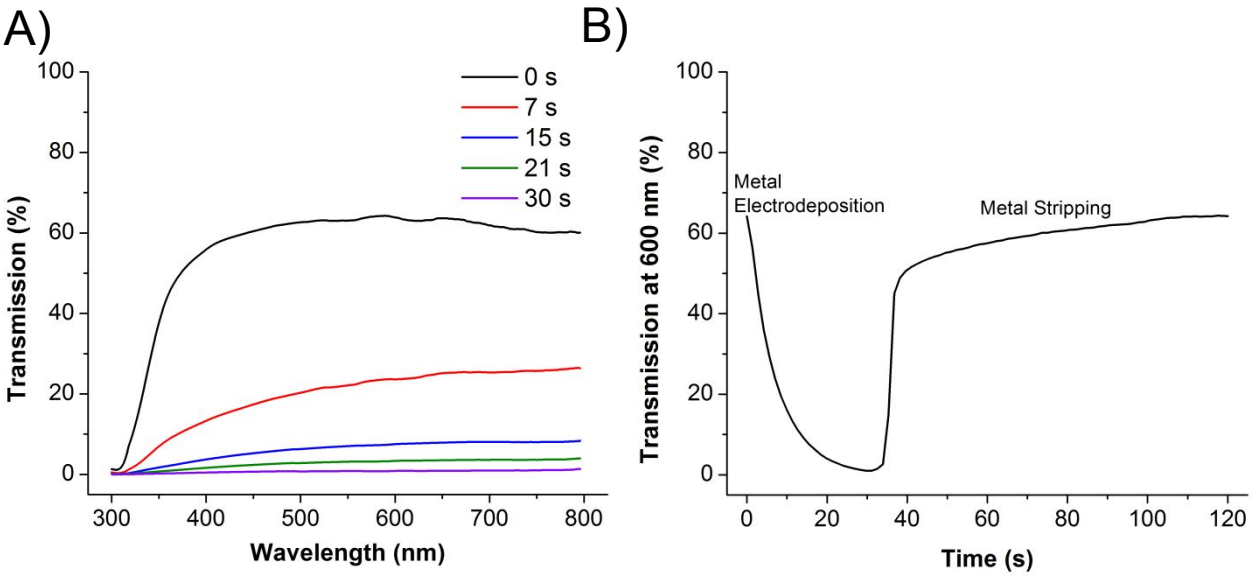

Figure 10: Transmission as a function of wavelength of a 25 cm^2 dynamic window based on reversible Zn electrodeposition after 0 s (black line), 7 s (red line), 15 s (blue line), 21 s (green line), and 30 s (purple line) of device darkening (A). Metal electrodeposition on the working electrode was elicited by applying -0.8 V for 30 s before +2.3 V was applied to induce metal stripping (Figure S7). The transmission at 600 nm during one cycle of switching is shown in panel B. The aqueous-based gel electrolyte used contained 0.5 M sodium formate, 0.25 M $ZnCl_2$, and 0.25 M $ZnBr_2$.

The application of -0.8 V for 30 s to the 25 cm^2 device causes the initial visible light transmission of the window to decrease from ~60% to <0.1% (Figure 10A). The high opacity of the window in its dark state is enabled by the dense morphology of the Zn electrodeposits on the ITO surface, which blocks light effectively. In its opaque state, the window appears black due to

its flat transmission profile across the visible spectrum. Additionally, the window in its opaque state effectively blocks near-infrared light, which is desirable for building applications in which heat management is important. After 30 s of metal electrodeposition on the working electrode, switching the voltage of the device to +2.3 V elicits rapid metal stripping, which causes the device to return to its original clear state within 90 s (Figure 10B). In its opaque state, the device exhibits good resting stability. When the device is switched to 1% transmission at 600 nm, its transmission remains below 5% over the course of 24 hours without the application of any voltage (Figure S8).

An important attribute of any dynamic window technology is device cycle life. Thus far, several different variants of dynamic windows based on reversible metal electrodeposition have been developed that cycle thousands of times without significant degradation.[24, 25, 31] Figure 11 displays the minimum and maximum transmission values of a dynamic window based on reversible Zn electrodeposition during consecutive switching cycles. From the data, it is clear that the maximum transmission value of the device steadily decreases over the course of 250 cycles. This less-than-optimal cycleability is in contrast to our previous work showing excellent cycle lives in windows using reversible Bi and Cu electrodeposition.

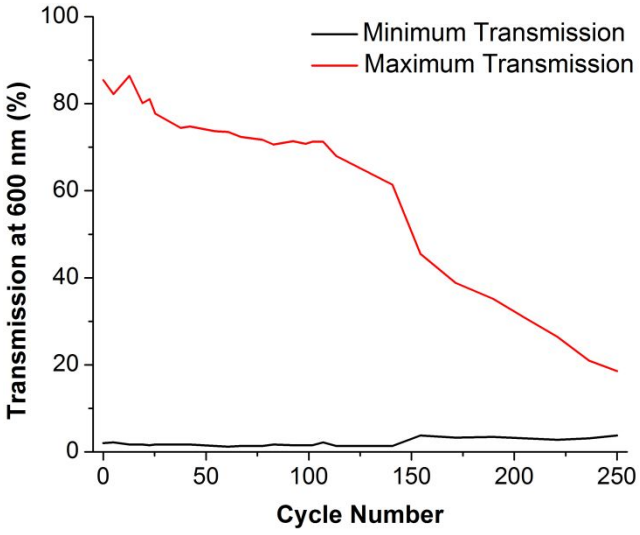

Figure 11: Minimum and maximum transmission values at 600 nm during cycling of a 3 cm^2 dynamic window based on Zn electrodeposition. The device was switched at -1 V for 5 s to induce metal electrodeposition and 1.5 V for 30 s to elicit metal stripping.

To understand the origin of the decrease in the maximum transmission value during cycling of the Zn windows, we conducted XRD on the working electrode after the 250 switching cycles. The XRD spectrum shows a prominent peak that is due to the presence of $Zn(OH)_2$. Because the intensity of this peak is much larger than any $Zn(OH)_2$ peak observed after one cycle of Zn electrodeposition, this finding suggests that $Zn(OH)_2$ progressively accumulates on the working electrode and is responsible for the steady decrease in the transparency of the window in its clear state during cycling.

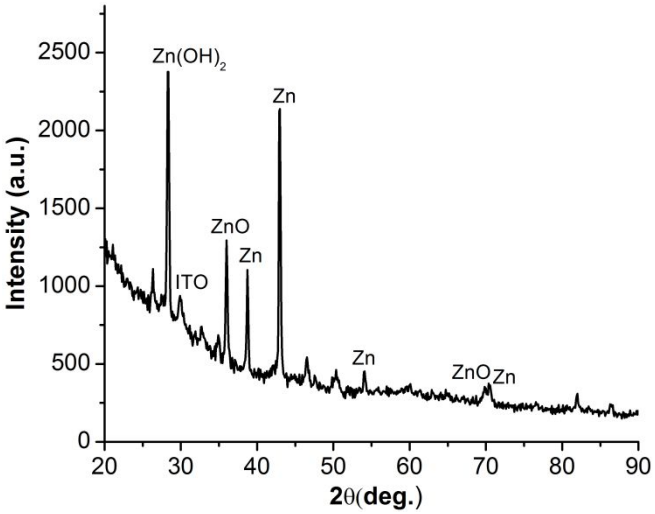

Figure 12: X-ray diffraction spectrum of ITO working electrode obtained after 250 switching cycles in a dynamic window.

In future work, we will carefully interrogate the origin of this accumulation of $Zn(OH)_2$ during cycling, and we will pursue several strategies to mitigate this problem including utilizing different voltage switching profiles and chemical additives such as chelating ligands that may facilitate $Zn(OH)_2$ dissolution. However, the focus on this manuscript is to interrogate the physicochemical parameters that allow for reversible Zn electrodeposition electrolytes, not to

develop practical windows or optimal cycling parameters. Nonetheless, because the design of such electrolytes is still in its infancy, we are hopeful that future versions of these electrolytes will enable the construction of robust and practical dynamic windows.

Conclusions

In this manuscript, we investigated a variety of chemical and physical properties of reversible Zn electrodeposition on transparent conducting electrodes. In particular, we systematically studied the effect of the chain length of carboxylates, the halogen in haloacetate, and the identity of supporting halides on the electrochemical reversibility of Zn electrolytes. These studies enabled us to develop electrolytes that are both optically and electrochemical reversibility (Coulombic efficiency up to 99%). Using SEM and XRD analysis, we correlated electrolyte composition with electrodeposit morphology and composition, both of which effect the reversibility of the system. We also discovered how reversible Zn electrodeposition occurs in these electrolytes despite the fact that electrode degradation and H_2 production are thermodynamically favorable within the voltage regimes need to elicit Zn electrodeposition. Lastly, we applied these findings to the construction of practical 25 cm^2 dynamic windows based on reversible Zn electrodeposition.

Conflicts of Interests

The authors have filed a provisional patent application related to his work, but there are no other conflicts of interests to declare.

Acknowledgements

This research was funded by Research and Innovation at the University of Nevada, Reno (UNR). We also acknowledge the Share Instrumentation Laboratory in the Department of Chemistry at UNR. We gratefully acknowledged the support of National Science Foundation (CHE-1429768)

for purchasing X-ray diffractometer. SEM-EDX analysis was performed in the Mackay Microbeam Laboratory at UNR, and we thank J. Desormeau for his kind assistance.

Footnote

Electronic supplementary information (ESI) available.

References

1. U.S. Energy Information Administration, Consumption & Effiency, 2018, https://www.eia.gov/consumption/, accessed February 17, 2021.
2. E. S. Lee, M. Yazdanian and S. E. Selkowitz, *Lawrence Berkeley National Laboratory*, 2004, LBNL-54966.
3. Energy Savings Guide, https://view.com/sites/default/files/documents/product-guide.pdf, (accessed February 17, 2021).
4. C. G. Granqvist, *Handbook of Inorganic Electrochromic Materials*, Elsevier, Amsterdam, 1995.
5. C. G. Granqvist, *Sol. Energ. Mat. Sol. C.*, 2000, **60**, 201-262.
6. G. A. Niklasson and C. G. Granqvist, *J. Mat. Chem.*, 2007, **17**, 127-156.
7. P. Shi, C. M. Amb, E. P. Knott, E. J. Thompson, D. Y. Liu, J. Mei, A. L. Dyer and J. R. Reynolds, *Adv. Mater.*, 2010, **22**, 4949-4953.
8. V. K. Thakur, G. Ding, J. Ma, P. S. Lee and X. Lu, *Adv. Mater.*, 2012, **24**, 4071-4096.
9. X. Li, Z. Wang, K. Chen, D. Y. Zemlyanov, L. You and J. Mei, *ACS Appl. Mater. Int.*, 2021, **13**, 5312-5318.
10. R. J. Mortimer, A. L. Dyer and J. R. Reynolds, *Displays*, 2006, **27**, 2-18.
11. G. Garcia, R. Buonsanti, A. Llordes, E. L. Runnerstrom, A. Bergerud and D. J. Milliron, *Adv. Opt. Mater.*, 2013, **1**, 215-220.
12. D. Coates, *J. Mat. Chem.*, 1995, **5**, 2063-2072.
13. J. W. Doane, A. Golemme, J. L. West, J. B. Whitehead and B. G. Wu, *Mol. Cryst. Liq. Crys.*, 1988, **165**, 511-532.
14. Y. Cui, Y. Ke, C. Liu, Z. Chen, N. Wang, L. Zhang, Y. Zhou, S. Wang, Y. Gao and Y. Long, *Joule*, 2018, **2**, 1707-1746.
15. M. Aburas, H. Ebendorff-Heidepriem, L. Lei, M. Li, J. Zhao, T. Williamson, Y. Wu and V. Soebarto, *Energ. Buildings*, 2021, **235**, 110717.
16. X. Tao, D. Liu, J. Yu and H. Cheng, *Adv. Opt. Mater.*, 2021, 2001847.
17. O. S. Heavens, *Optical Properties of Thin Solid Films*, Dover Publications, Inc., New York, 1965.
18. N. N. Greenwood and A. Earnshaw, *Chemistry of the Elements*, Butterworth-Heinemann, Oxford, U. K., 2nd ed., 1997.
19. G. K. A. Alcaraz, J. S. Juarez-Rolon, N. A. Burpee and C. J. Barile, *J. Mat. Chem. C*, 2018, **6**, 2132-2138.
20. S. M. Islam, C. N. Fini and C. J. Barile, *J. Electrochem. Soc.*, 2019, **166**, D333-D338.
21. C. J. Barile, *J. Appl. Electrochem.*, 2018, **48**, 443-449.
22. J. P. Ziegler, *Sol. Energ. Mat. Sol. C.*, 1999, **56**, 477-493.

23. M. T. Strand, C. J. Barile, T. S. Hernandez, T. E. Dayrit, L. Bertoluzzi, D. J. Slotcavage and M. D. McGehee, *ACS Energ. Lett.*, 2018, **3**, 2823-2828.
24. T. S. Hernandez, M. Alshurafa, M. T. Strand, A. L. Yeang, M. G. Danner, C. J. Barile and M. D. McGehee, *Joule*, 2020, **4**, 1501-1513.
25. S. M. Islam, T. S. Hernandez, M. D. McGehee and C. J. Barile, *Nat. Energ.*, 2019, **4**, 223-229.
26. S. M. Islam and C. J. Barile, *ACS Appl. Mater. Inter.*, 2019, **11**, 40043-40049.
27. S. M. Islam, A. A. Palma, R. P. Gautam and C. J. Barile, *ACS Appl. Mater. Inter.*, 2020, **12**, 44874-44882.
28. S. Araki, K. Nakamura, K. Kobayashi, A. Tsuboi and N. Kobayashi, *Adv. Mater.*, 2012, **24**, OP122-OP126.
29. A. Tsuboi, K. Nakamura and N. Kobayashi, *Adv. Mater.*, 2013, **25**, 3197-3201.
30. C. Park, S. Seo, H. Shin, B. D. Sarwade, J. Na and E. Kim, *Chem. Sci.*, 2015, **6**, 596-602.
31. C. J. Barile, D. J. Slotcavage, J. Hou, M. T. Strand, T. S. Hernandez and M. D. McGehee, *Joule*, 2017, **1**, 133-145.
32. J. Y. Li, J. S. Juarez-Rolon, S. M. Islam and C. J. Barile, *J. Electrochem. Soc.*, 2019, **166**, D496-D504.
33. T. S. Hernandez, C. J. Barile, M. T. Strand, T. E. Dayrit, D. J. Slotcavage and M. D. McGehee, *ACS Energ. Lett.*, 2018, **3**, 104-111.
34. P. Vanysek, *Electrochemical Series*, Boca Raton, FL, 83rd edn., 2002.
35. H. Li, W. Zhang and A. Y. Elezzabi, *Adv. Mater.*, 2020, **32**, 2003574.
36. K. Kondo, H. Kouta, M. Yokoi, N. Okamoto, T. Saito and T. Hayashi, *ECS Trans.*, 2014, **58**, 89-96.
37. M. Schlesinger and M. Paunovic, *Modern Electroplating*, John Wiley, Hoboken, NJ, 5th ed., 2010.
38. Y. R. Luo, *Comprehensive Handbook of Chemical Bond Energies*, CRC Press, Taylor & Francis Group, Boca Raton, FL, 2007.39. W. S. M. Werner, K. Glantschnig and C. Ambrosch-Draxl, *J. Phys. Chem. Ref. Data*, 2009, **38**, 1013-1092.
40. H. Yoshikawa and S. Adachi, *Jpn. J. Appl. Phys.*, 1997, **36**, 6237-6243.
41. J. D. Benck, B. A. Pinaud, Y. Gorlin and T. F. Jaramillo, *PlOS One*, 2014, **9**, e107942-e107942.
42. P. Quaino, F. Juarez, E. Santos and W. Schmickler, *Bellstein J. Nanotech.*, 2014, **5**, 846-854.